

Scalable Spatiotemporal Prediction with Bayesian Neural Fields

Feras Saad^{1,2*}, Jacob Burnim², Colin Carroll², Brian Patton²,
Urs Köster², Rif A. Saurous², Matthew Hoffman²

¹Computer Science Department, Carnegie Mellon University, 5000 Forbes Ave,
Pittsburgh, PA 15213, USA.

²Google Research, 1600 Amphitheatre Pkwy, Mountain View, CA 10587, USA.

*Corresponding author(s). E-mail(s): fsaad@cmu.edu;

Contributing authors: jburnim@google.com; colcarroll@google.com;
bjp@google.com; ursk@google.com; rif@google.com; mhoffman@google.com;

Abstract

Spatiotemporal datasets, which consist of spatially-referenced time series, are ubiquitous in many scientific and business-intelligence applications, such as air pollution monitoring, disease tracking, and cloud-demand forecasting. As modern datasets continue to increase in size and complexity, there is a growing need for new statistical methods that are flexible enough to capture complex spatiotemporal dynamics and scalable enough to handle large prediction problems. This work presents the Bayesian Neural Field (BAYESNF), a domain-general statistical model for inferring rich probability distributions over a spatiotemporal domain, which can be used for data-analysis tasks including forecasting, interpolation, and variography. BAYESNF integrates a novel deep neural network architecture for high-capacity function estimation with hierarchical Bayesian inference for robust uncertainty quantification. By defining the prior through a sequence of smooth differentiable transforms, posterior inference is conducted on large-scale data using variationally learned surrogates trained via stochastic gradient descent. We evaluate BAYESNF against prominent statistical and machine-learning baselines, showing considerable improvements on diverse prediction problems from climate and public health datasets that contain tens to hundreds of thousands of measurements. The paper is accompanied with an open-source software package (<https://github.com/google/bayesnf>) that is easy-to-use and compatible with modern GPU and TPU accelerators on the JAX machine learning platform.

Keywords: spatiotemporal prediction, Bayesian inference, deep neural networks, geostatistics

1 Introduction

Spatiotemporal data, which consists of measurements gathered at different times and locations, is ubiquitous across diverse disciplines. Government bodies such as the European Environment Agency¹ and United States Environmental Protection Agency², for example, routinely monitor a variety of air quality indicators (PM₁₀, NO₂, O₃, etc.) in order to understand their ecological and public health impacts [1, 2]. As it is physically impossible to place sensors that record measurements and all locations and time points within a large geographic area, a central problem faced by environmental data scientists is developing models that can predict these indicators at novel locations or time points at which no measurements exist [3, 4]. Spatiotemporal data analysis also plays an important role in cloud computing, where consumer demand for resources such as CPU, RAM, and storage is driven by time-evolving macroeconomic factors and varies drastically across data center location. Cloud service providers develop sophisticated demand-forecasting models to determine prices [5], perform load balancing [6], save energy [7], and achieve service level agreements [8]. Additional applications of spatiotemporal data analysis include meteorology (forecasting rain volume [9] or wind speeds [10]), epidemiology (“nowcasting” active flu cases [11]), and urban planning (predicting rider congestion patterns at metro stations [12]).

Unlike traditional regression or classification methods in machine learning that operate on independent and identically distributed (i.i.d.) data, accurate models of spatiotemporal data must capture complex and highly nonstationary dynamics in both the time and space domain. For example, two locations twenty miles apart in California’s central valley may exhibit nearly identical temperature patterns, whereas two locations only one mile apart in nearby San Francisco might have very different microclimates; and these effects may differ depending on the time of year. Handling such variability across different scales is a key challenge in designing accurate statistical models. Another challenge is that spatiotemporal observations are almost always driven by unknown data-generating processes that produce noisy outputs, which requires models that report probabilistic predictions to account for the aleortic and epistemic uncertainty in the data.

Probabilistic Models of Spatiotemporal Data. The dominant approach to spatiotemporal data modeling in statistics rests on *Gaussian processes*, a rich class of Bayesian nonparametric priors on random functions [13–15]. Consider a spatiotemporal field $Y(\mathbf{s}, t)$ indexed by spatial locations $\mathbf{s} \in \mathbb{R}^d$ and time points $t \in \mathbb{R}$. A typical Gaussian-process based “prior probability” distribution (used in popular geostatistical software packages such as R-INLA [16] and sdm-TMB [17]) over the data-generating process for the random field Y is given by:

$$\eta \sim \text{GP}(0, k_\theta); \quad F(\mathbf{s}, t) = h(x(\mathbf{s}, t); \beta) + \eta(\mathbf{s}, t); \quad Y(\mathbf{s}, t) \sim \text{Dist}(g(F(\mathbf{s}, t)), \gamma). \quad (1)$$

In Eq. (1), η is a random function whose covariance over space and time is determined by a *kernel function* $k_\theta((\mathbf{s}, t), (\mathbf{s}', t'))$ parameterized by θ ; $x(\mathbf{s}, t)$ is a covariate vector associated with index (\mathbf{s}, t) ; h is a mean function with parameters β (e.g., for a linear function, $h(x; \beta) := \beta'x$) of the latent field F ; and Dist is a noise model (e.g., Normal, Poisson) for the observations $Y(\mathbf{s}, t)$, with index-specific parameter $g(F(\mathbf{s}, t))$ (where g is a link function, e.g., \exp) and global parameters γ .

Given an observed dataset $\mathcal{D} := \{Y(\mathbf{s}_1, t_1) = y_1, \dots, Y(\mathbf{s}_N, t_N) = y_N\}$, the inference problem is to determine the unknown parameters (θ, β, γ) , which in turn define a *posterior distribution* over the processes (η, F, Y) given \mathcal{D} . Advantages of the model (1) are its flexibility (as η is capable of representing highly complex covariance structure) and ability to handle uncertainty quantification (the posterior spreads its probability mass over a range of functions and model parameters that are consistent with the data). Moreover, the model easily handles arbitrary patterns of missing data by treating them as latent variables. A number of recent articles have developed specialized Gaussian process techniques for modeling rich spatiotemporal fields [e.g., 17–21].

¹<https://airindex.eea.europa.eu/>

²<https://airnow.gov/>

Key Challenges. Despite their flexibility, spatiotemporal models such as Eq. (1) based on Gaussian processes come with significant challenges. The first is computational. The simplest and most accurate posterior inference algorithms for these models have a computational cost of $O(N^3)$, where N is the number of observations, which is unacceptably high in datasets with tens or hundreds of thousands of observations. Reducing this cost requires compromises, either on the modeling side (e.g., imposing a discrete Markovian structure on the model [16, 17]) or on the posterior-inference side (e.g., approximating the true posterior with a simpler Gaussian process [18, 19, 21]). Either way, the resulting models have less expressive power and cannot explain the data as accurately. These approximations also involve delicate linear-algebraic derivations or stochastic differential equations, which are challenging to implement and apply to new settings.

The second challenge is expertise, where the accuracy of model (1) on a given dataset is dictated by key choices such as the covariance kernel k_θ and mean function h . Even for seasoned data scientists, designing these quantities is difficult because it requires detailed knowledge about the application domain. Further, even small modifications to the model can impose large changes to the learning algorithm, and so most software packages only support a small set of predetermined covariance structures k_θ (e.g., separable Matérn kernels, radial basis kernel, polynomial kernel) that are optimized enough to work effectively on large datasets.

In light of these challenges, researchers have been developing new spatiotemporal techniques that combine deep neural networks with multilevel Gaussian process models. Wikle and Zammit-Mangion [22] provide a thorough survey of these advances and their advantages in flexibility or scalability over the standard model (1). Despite these improvements, however, these approaches may lack certain attractive affordances of Gaussian processes, for example: (i) Bayesian spatiotemporal recurrent neural networks [23] assume that the data is observed at a fixed spatial grid and regular discrete-time intervals; (ii) deep “Empirical Orthogonal Function” models [24] cannot handle missing data, make predictions at new time points, or deliver uncertainty estimates; and (iii) deep neural network warpings of inputs to Gaussian processes [25] include hard-to-tune decisions about how to order the observations and how to define their nearest-neighbor sets.

This Work. To alleviate these fundamental tensions, this article introduces the *Bayesian Neural Field* (BAYESNF)—a novel method that combines the scalability of deep neural networks with many of the attractive properties of Gaussian processes. BAYESNF is built on a Bayesian neural network model [26] that maps from multivariate space-time coordinates to a real-valued field. The parameters of the network are assigned a prior distribution, and as in Gaussian processes, conditioning on observed data induces a posterior over those parameters (and in turn over the entire field). Because inference is performed in “weight space” rather than “function space”, the cost of analyzing a dataset grows linearly with the number of observations, as opposed to cubically for a Gaussian process. Because BAYESNF is a hierarchical model (Fig. 1), it naturally handles missing data as latent variables and quantifies uncertainty over parameters and predictions. And because BAYESNF defines a field over continuous space-time, can model non-uniformly sampled data, interpolate in space, and extrapolate in time to make predictions at novel coordinates.

Our description of BAYESNF as a neural “field” is inspired by the recent literature on neural radiance fields [NeRFs; 27, 28] in computer vision. A key discovery that enabled the success of NeRFs is that neural networks are biased towards learning functions whose Fourier spectra are dominated by low frequencies, and that this bias can be corrected by concatenating sinusoidal positional encodings to the raw spatial inputs [29]. Likewise, our results show that Fourier features enable BAYESNF models to learn flexible and well-calibrated distributions of spatiotemporal data; and that incorporating sinusoidal seasonality features lets BAYESNF models make predictions based on (multiple) seasonal effects as well. Taken together, these characteristics enable state-of-the-art performance in terms of point predictions and 95% prediction intervals on diverse large-scale spatiotemporal datasets, without the need to heavily customize the BAYESNF model structures on a per-dataset basis.

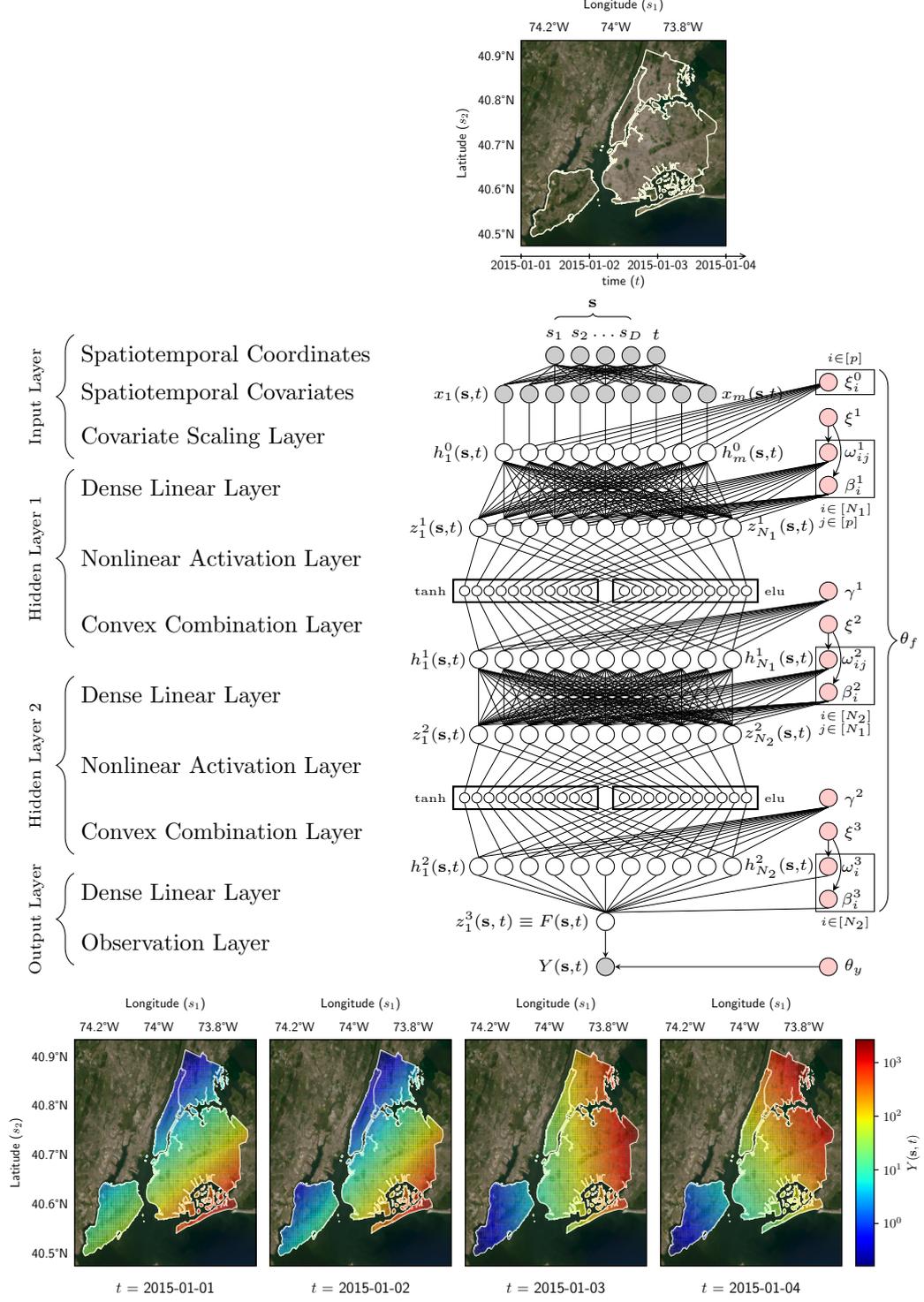


Fig. 1 Top: Example of a spatiotemporal domain with two spatial coordinates (latitude, longitude) and a daily time coordinate. Middle: BAYESNF represented as a probabilistic graphical model. Each node is a model variable and each edge is a direct relationship between a pair of variables. Gray nodes are observed variables, which are both associated with an observation $Y(\mathbf{s}, t)$ at a spatiotemporal coordinate (\mathbf{s}, t) . Pink nodes are global latent variables (parameters) that are shared across all spatiotemporal coordinates. Bottom: Realizations of the spatiotemporal field generated from the BAYESNF, at four example time points.

Configuration: H : no. of internal layers; $[x_1(\cdot), \dots, x_m(\cdot)]$: covariates;
 N_d, A_d : no. of hidden units and activation functions ($1 \leq d \leq H$);
 u_j^d : activation functions ($1 \leq d \leq H; 1 \leq j \leq A_d$)

Covariate Scaling Layer:

$$(\xi_1^0, \dots, \xi_m^0) \stackrel{\text{iid}}{\sim} N(0, 1) \quad h^0(\mathbf{s}, t) := (e^{\xi_1^0} x_1(\mathbf{s}, t), \dots, e^{\xi_m^0} x_m(\mathbf{s}, t))$$

Hidden Layers: $d = 1, \dots, H + 1, i = 1, \dots, N_d$

$$(\xi^d, \gamma_1^d, \dots, \gamma_{A_d}^d) \stackrel{\text{iid}}{\sim} N(0, 1), \quad z_i^d(\mathbf{s}, t) := \sum_{j=1}^{N_{d-1}} \frac{\omega_{ij}^d}{\sqrt{N_{d-1}}} h_j^{d-1}(\mathbf{s}, t) + \beta_i^d$$

$$(\omega_{i1}^d, \dots, \omega_{iN_{d-1}}^d, \beta_i^d) \stackrel{\text{iid}}{\sim} N(0, \sigma_d^2) \quad h_i^d(\mathbf{s}, t) := \sum_{j=1}^{A_d} \frac{e^{\gamma_j^d}}{\sum_{k=1}^{A_d} e^{\gamma_k^d}} u_j^d(z_i^d(\mathbf{s}, t))$$

where $\sigma_d := \ln(1 + e^{\xi^d})$ (only if $d < H + 1$)

Observation Layer:

$$\Theta_y \sim \pi_y \quad F(\mathbf{s}, t) := z_1^{H+1}(\mathbf{s}, t)$$

$$Y(\mathbf{s}, t) \sim \text{Dist}(F(\mathbf{s}, t), \Theta_y)$$

Listing 1 Generative process for the Bayesian Neural Field in Fig. 1. Terms on the left are global parameters. Terms on the right are local latent variables indexed by a spatiotemporal index (\mathbf{s}, t) .

2 Results

2.1 Model Description

Suppose we are given a dataset $\mathcal{D} = \{y(\mathbf{s}_i, t_i) \mid i = 1, \dots, N\}$ of N spatiotemporal observations, where $\mathbf{s}_i \in \mathcal{S} \subset \mathbb{R}^d$ denotes a d -dimensional spatial coordinate and $t_i \in \mathcal{T} \subset \mathbb{R}$ denotes a time index. For example, if the field is observed at longitude-latitude coordinates in discrete time, then $\mathcal{S} = (-180, 180] \times [-90, 90] \subset \mathbb{R}^2$ and $\mathcal{T} = \{1, 2, \dots\}$. If the field also incorporates an altitude dimension, then $\mathcal{S} \subset \mathbb{R}^3$. We model this dataset as a realization $\{Y(\mathbf{s}_i, t_i) = y(\mathbf{s}_i, t_i), 1 \leq i \leq n\}$ of a random field $Y : \mathcal{S} \times \mathcal{T} \rightarrow \mathbb{R}$ over the entire spatiotemporal domain. Following the notation in Wikle and Zammit-Mangion [22], we describe the field using a hierarchical Bayesian model:

$$\text{Observation Model: } [Y(\cdot) \mid F(\cdot), \Theta_y], \quad (2)$$

$$\text{Process Model: } [F(\cdot) \mid x(\cdot), \Theta_f], \quad (3)$$

$$\text{Parameter Models: } [\Theta_y, \Theta_f]. \quad (4)$$

In this notation, upper case letters denote random quantities, Greek letters denote model parameters, lower case letters denoted non-random (fixed) quantities, and square brackets $[\cdot]$ denote (yet-to-specified) probability distributions. The distribution of the observable random variables $Y(\mathbf{s}, t)$ is parameterized by global parameters Θ_y and an unobservable (latent) spatiotemporal field $F(\mathbf{s}, t)$. In turn, $F(\mathbf{s}, t)$ is parameterized by a set of random global parameters Θ_f and a collection $x(\mathbf{s}, t) = [x_1(\mathbf{s}, t), \dots, x_m(\mathbf{s}, t)]$ of m fixed covariates associated with index (\mathbf{s}, t) .

Listing 1 completes the definition of BAYESNF by showing specific probability distributions for the model (2)–(4). Figure 1 shows a probabilistic-graphical-model representation of a BAYESNF model with $H = 3$ layers, which takes a spatiotemporal index (\mathbf{s}, t) at the input layer and generates a realization $Y(\mathbf{s}, t)$ of the observable field at the output layer. We next describe the components of this process in sequence from inputs to outputs. Note that we are describing a

Table 1 Examples of seasonal features for BAYESNF. Each entry denotes the period p corresponding to a measurement frequency and seasonal effect. Given a period p and time point t , the seasonal features are $[\cos(2\pi h/pt), \sin(2\pi h/pt)]$ for harmonics $h = 1, \dots, p/2$.

		Seasonal Effect							
		Secondly	Minutely	Hourly	Daily	Weekly	Monthly	Quarterly	Yearly
Measurements	Yearly	–	–	–	–	–	–	–	1
	Quarterly	–	–	–	–	–	–	1	4
	Monthly	–	–	–	–	–	1	3	12
	Weekly	–	–	–	–	1	4.35	13.045	52.18
	Daily	–	–	–	1	7	30.44	91.32	365.25
	Hourly	–	–	1	24	168	730.5	2191.5	8766
	Minutely	–	1	60	1440	10080	43830	131490	525960
	Secondly	1	60	3600	86400	604800	2629800	7889400	31557600

prior distribution over Bayesian Neural Fields—in Section 4.1 we will discuss ways of inferring the *posterior* over the random variables defined in Listing 1.

Spatiotemporal Covariates. Letting $(\mathbf{s}, t) = ((s_1, \dots, s_d), t)$ denote a generic index in the field, the covariates $[x_1(\mathbf{s}, t), \dots, x_m(\mathbf{s}, t)]$ may include the following functions:

$$\{t, s_1, \dots, s_d\} \quad \text{Linear Terms} \quad (5)$$

$$\{ts_1, \dots, ts_d\} \quad \text{Temporal-Spatial Interactions} \quad (6)$$

$$\{s_i s_j; 1 \leq i < j \leq d\} \quad \text{Spatial-Spatial Interactions} \quad (7)$$

$$\{(\cos(2\pi h/pt), \sin(2\pi h/pt)); p \in \mathcal{P}, h \in \mathcal{H}_p^t\} \quad \text{Temporal Seasonal Features} \quad (8)$$

$$\{(\cos(2\pi 2^h s_i), \sin(2\pi 2^h s_i)); 1 \leq i \leq d, h \in \mathcal{H}_i^s\} \quad \text{Spatial Fourier Features} \quad (9)$$

The linear and interaction covariates (5)–(7) are the usual first and second-order effects used in spatiotemporal trend-surface analysis models [15, Sec. 3.2]. In Eq. (8), the temporal seasonal features are defined by a set $\mathcal{P} = \{p_1, \dots, p_\ell\}$ of ℓ seasonal periods, where each p_i has harmonics $\mathcal{H}_{p_i}^t \subset \{1, 2, \dots, \lfloor p_i/2 \rfloor\}$ for $i = 1, \dots, \ell$. Table 1 shows how to construct the periods given the time units and seasonal effects. For example, if the time unit is hourly data and there are $m = 2$ seasonal effects (daily and monthly), the corresponding periods are $p_1 = 24$ and $p_2 = 730.5$, respectively. Non-integer values in Table 1 account for the fact that certain seasonal effects have varying duration in the time measurement unit (e.g., days per month or weeks per year). In Eq. (9), the spatial Fourier features for coordinate s_i are determined by a set $\mathcal{H}_i^s \subset \mathbb{N}$ of additional frequencies that express periodic structure in the i -th dimension ($i = 1, \dots, d$). These covariates correct for the tendency of neural networks to learn low-frequency signals [29]: our empirical evaluation in Section 2.3 confirms that their presence improves the quality of learned BAYESNF models. The covariate vector $x(\mathbf{s}, t)$ may also include exogenous signals that are not derived from spatial or temporal coordinates (e.g., temperature), provided that these values are available for any index (\mathbf{s}, t) in the observed dataset or in the prediction set.

Covariate Scaling Layer. Scaling inputs improves neural network learning [e.g., 30], but determining the appropriate strategy (e.g., z-score, min/max, tanh, batch-norm, layer-norm, etc.) is challenging. BAYESNF uses a prior distribution over scale factors to learn these quantities as part of Bayesian inference within the overall probabilistic model. In particular, the next stage in the network is a width- m hidden layer $h_i^0(\mathbf{s}, t) = e^{\xi_i^0} x_i(\mathbf{s}, t)$ obtained by randomly scaling each of the m covariates $x(\mathbf{s}, t)$, where $e^{\xi_i^0}$ is a log-normally distributed scale factor (for $i = 1, \dots, m$).

Hidden Layers. The model contains $H + 1 \geq 1$ hidden layers, where layer d has N_d units $h^d = (h_1^d, \dots, h_{N_d}^d)'$ (for $d = 1, \dots, H$). These hidden units are derived from N_d *pre-activation*

units $z^d = N_{d-1}^{-1/2} \Omega^d h^{d-1} + \beta^d$ where $\Omega^d = [\omega_{ij}^d; 1 \leq i \leq N_d, 1 \leq j \leq N_{d-1}]$ is a random $N_d \times N_{d-1}$ weight matrix and $\beta^d = (\beta_1^d, \dots, \beta_{N_d}^d)'$ a random bias term. The ω_{ij}^d and β_i^d terms are drawn i.i.d. $N(0, \sigma_d^2)$, where $\sigma_d = \ln(1 + e^{\xi^d})$ is itself obtained by applying the smooth “softplus” transformation to $\xi^d \sim N(0, 1)$. The $N_{d-1}^{-1/2}$ prefactor is needed for the network to have a well-defined limit to a Gaussian process as the number of hidden units $N_d \rightarrow \infty$ [26].

BAYESNF departs from a traditional Bayesian neural network by using $A_d \geq 1$ activation functions $(u_1^d, \dots, u_{A_d}^d)$ at hidden layer d , instead of the usual $A_d = 1$. For example, the architecture shown in Fig. 1 uses $A_d = 2$ for $d \in \{1, 2\}$, where u_1^d is the hyperbolic tangent (tanh) and u_2^d is the exponential linear unit (elu) activation. Each *post-activation* unit h_i^d (for $i = 1, \dots, N_d$) is then a random convex combination of the activations $u_1^d(z_i^d), \dots, u_{A_d}^d(z_i^d)$, where the coefficient of u_j^d is the output of a softmax function $e^{\gamma_j^d} / \sum_{k=1}^{A_d} e^{\gamma_k^d}$ whose j -th input is $\gamma_j^d \sim N(0, 1)$ (for $j = 1, \dots, A_d$). By specifying the overall activation at each layer as a learnable convex combination of A_d “basic” activation functions (e.g., tanh, relu, elu), BAYESNF aims to automate the challenging process of selecting an appropriate activation function—which is known to govern the overall properties of the random function defined by a Bayesian neural network [26, 31].

Finally, the latent stochastic process $F(\mathbf{s}, t)$ is defined as the pre-activation unit z_1^{H+1} of layer $H + 1$, which has exactly $N_{H+1} = 1$ unit. We let Θ_f denote all n_f random network parameters in Listing 1, whose prior is π_f . Further, the notation $F_{\theta_f}(\mathbf{s}, t)$ denotes the (deterministic) value of the process F at index (\mathbf{s}, t) when $\Theta_f = \theta_f$.

Observation Layer. The final layer connects the stochastic process $F(\mathbf{s}, t)$ with the observable spatiotemporal field $Y(\mathbf{s}, t) \sim \text{Dist}(F(\mathbf{s}, t); \Theta_y)$ through a noise model that captures aleatoric uncertainty in the data. The parameter vector $\Theta_y = (\Theta_{y,1}, \dots, \Theta_{y,n_y})$ is n_y -dimensional and has a prior π_y . There are many choices for this distribution, depending on the field $Y(\mathbf{s}, t)$; for example,

$$Y(\mathbf{s}, t) \sim \text{Normal}(F(\mathbf{s}, t), \Theta_{y,1}) \quad (10)$$

$$Y(\mathbf{s}, t) \sim \text{StudentT}_{\Theta_{y,2}}(F(\mathbf{s}, t), \Theta_{y,1}) \quad (11)$$

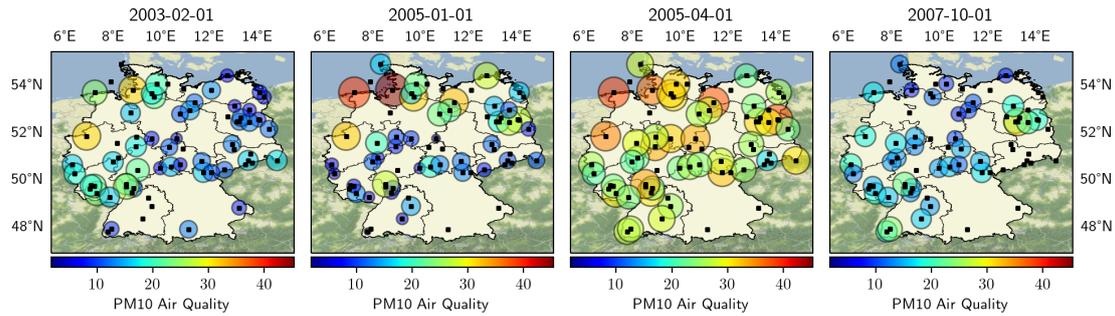
$$Y(\mathbf{s}, t) \sim \text{Poisson}(e^{F(\mathbf{s}, t)}), \quad (12)$$

which correspond to a Gaussian noise model with mean $F(\mathbf{s}, t)$ and variance $\Theta_{y,1}$ ($n_y = 1$), a StudentT model with location $F(\mathbf{s}, t)$, scale $\Theta_{y,1}$ and $\Theta_{y,2}$ degrees of freedom ($n_y = 2$); and a Poisson counts model with rate $\exp F(\mathbf{s}, t)$ ($n_y = 0$), respectively.

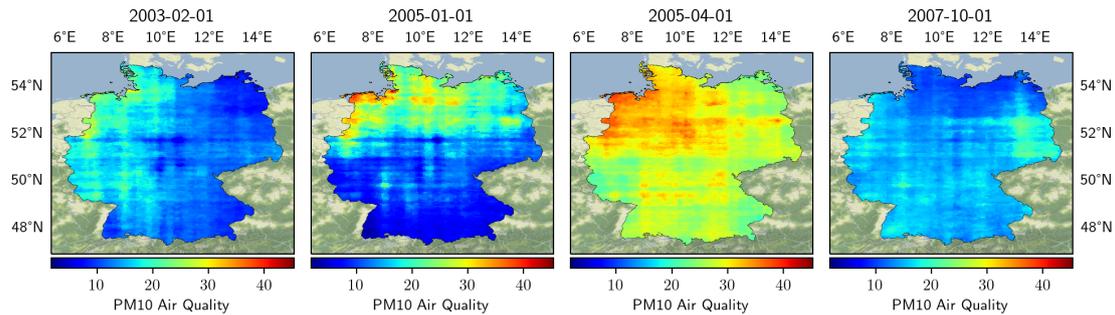
Posterior Inference and Querying. Let $P(\Theta_f, \Theta_y, Y)$ be the joint probability distribution over the parameters and observable field in Listing 1. The posterior distribution given \mathcal{D} is

$$\begin{aligned} & P(\theta_f, \theta_y \mid \{Y(\mathbf{s}_i, t_i) = y(\mathbf{s}_i, t_i)\}_{i=1}^N) \\ & \propto \left(\prod_{i=1}^{n_f} \pi_f(\theta_{f,i}) \right) \left(\prod_{i=1}^{n_y} \pi_y(\theta_{y,i}) \right) \prod_{i=1}^n \text{Dist}(y(\mathbf{s}_i, t_i); F_{\theta_f}(\mathbf{s}_i, t_i), \theta_y) \end{aligned} \quad (13)$$

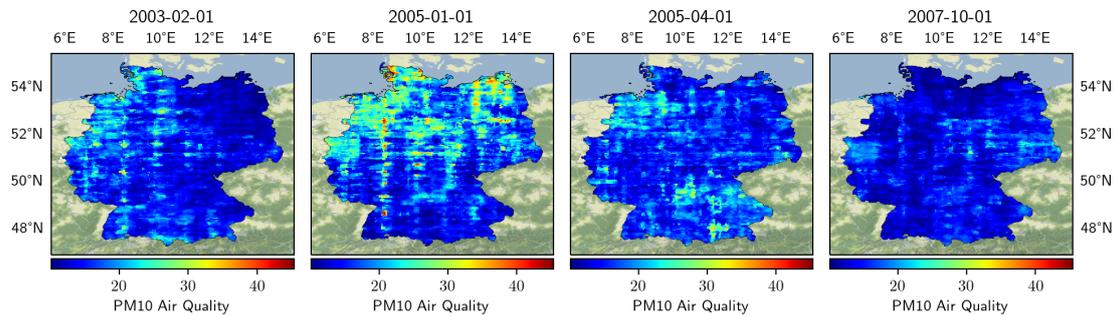
While the right-hand side of Eq. (13) is tractable to compute, the left-hand side cannot be normalized or sampled from exactly. Section 4.1 discusses two approximate posterior inference algorithms for BAYESNF: maximum-a-posterior ensembles and variational inference ensembles. They each produce a collection of parameters $\{(\theta_f^i, \theta_y^i)\}_{i=1}^M \approx P(\Theta_f, \Theta_y \mid \mathcal{D})$ drawn from an approximation to the posterior (13). Section 4.2 discusses how these posterior samples be used to compute *point predictions* $\hat{y}(\mathbf{s}_*, t_*)$ of the spatiotemporal field at a novel index (\mathbf{s}_*, t_*) and the associated *prediction intervals* $[\hat{y}_{\text{low}}(\mathbf{s}_*, t_*), \hat{y}_{\text{hi}}(\mathbf{s}_*, t_*)]$ for a given level $\alpha \in (0, 1)$ (e.g., $\alpha = 95\%$).



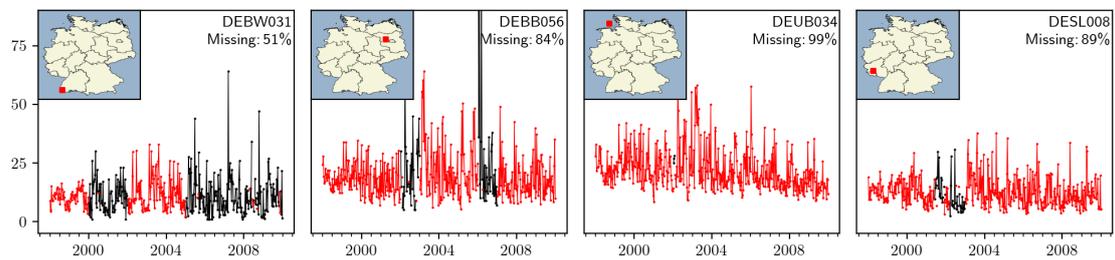
(a) Observations of PM10 air quality in Germany at four time points and 70 locations.



(b) Median predictions of PM10 air quality at four time points across the whole spatial field.



(c) Width of 95% predictions of PM10 air quality at four time points across the whole spatial field.



(d) Observed PM10 data (black) and median prediction (red) at four sparsely observed locations across time.

Fig. 2 Spatiotemporal prediction of atmospheric particulate matter (PM10) in German air dataset. (a) shows the observed data at four time points: each shaded circle represents a measurements of PM10 at a given station. Higher values of PM10 correspond to lower air quality. The data is sparse: at any given time point, only 47% of stations (on average) are associated with a PM10 observation. (b)–(d) show predictions across space and time.

2.2 Analyzing German Air Quality Data

Atmospheric particulate matter (PM10) is an important indicator of air quality used by governments worldwide. Airborne particles with a diameter of 10 microns or less are inhalable into the lungs and can induce adverse health effects. The ability to accurately predict PM10 values at novel points in space and time within a geographic region helps characterize pollution patterns and inform public health decisions.

We explore predictions from BAYESNF on the German Air Quality dataset [32], which contains daily PM10 measurements from 70 stations between 1998-01-01 and 2009-12-31. We infer a BAYESNF model for this dataset with depth $H = 2$; weekly, monthly, and yearly seasonal effects (8) (c.f. Table 1); and harmonics $\mathcal{H}_1^s = \mathcal{H}_2^s = \{1, \dots, 4\}$ for the spatial Fourier features (9). The distribution of Y given the stochastic process F is a StudentT (11) truncated to $\mathbb{R}_{\geq 0}$

Spatial and Temporal Interpolation

Figure 2a shows the PM10 observations at 2003-02-01, 2005-01-01, 2005-04-01, and 2007-01-01, where roughly 50% of the stations do not have an observed measurement at a given point in time. Figure 2b shows the median PM10 predictions $y_{0.5}(\mathbf{s}_*, t_*)$ (23) interpolated at a grid of 10,000 novel spatial indexes (\mathbf{s}_*, t_*) within Germany. Figure 2c shows the width $\hat{y}_{\text{hi}}(\mathbf{s}_*, t_*) - \hat{y}_{\text{low}}(\mathbf{s}_*, t_*)$ of the inferred 95% prediction interval. These plots reflect the nontrivial spatiotemporal structure captured by BAYESNF across space and time and identify coordinates within the field with low and high predictive uncertainty about air pollution.

Figure 2d shows the observed and median predicted PM10 values across all time points at four stations with the highest missing data rates: DEBWO31, southwest Germany, 51% missing; DEBB056, northeast Germany, 84% missing; DEBU034, northwest Germany, 99% missing; DESL008, west Germany, 89% missing. PM10 trajectories predicted by BAYESNF at time points where data is missing reproduce the temporal patterns at time points with observed data, which include high frequency periodic variation and irregular, spatially correlated jumps.

Variography

The accuracy of PM10 predictions in Fig. 2d cannot be quantitatively assessed because the ground-truth values are not known at the predicted time points. However, we can assess how well the learned spatiotemporal field matches the observed field by comparing the empirical and inferred semi-variograms. The semi-variogram γ of a process Y characterizes the joint spatiotemporal dependence structure; it is defined as

$$2\gamma(\mathbf{h}, \tau) = \text{Var}[Y(\mathbf{s} + \mathbf{h}, t + \tau) - Y(\mathbf{s}, t)] \quad (\mathbf{h} \in \mathcal{S}, \tau \in \mathcal{T}), \quad (14)$$

where the choice of $\mathbf{s} \in \mathcal{S}, t \in \mathcal{T}$ is arbitrary (e.g., $(\mathbf{s}, t) = (\mathbf{0}, 0)$), under the assumption that only the displacements in time and space affect the dependence [15, Sec. 2.4.2].

The surface plots in Fig. 3 compare the empirical semi-variogram (left) computed at the 70 observed stations with the inferred semi-variogram (right) computed at 70 uniformly chosen random indexes within Germany, for distances $\mathbf{h} \in [0, 1000]$ kilometers and time lags $\tau \in \{0, \dots, 10\}$ days. The agreement between these two plots confirms that BAYESNF accurately generalizes the spatiotemporal dependence structure from the observed locations to novel locations in the field. The lower two panels in Fig. 3 show the empirical (solid line) and inferred (dashed line) semi-variograms, separately for each of the 10 time lags τ . The difference between the semi-variograms is highest for $\tau \in \{0, 1, 2\}$ days, suggesting that the learned model is expressing relatively smooth phenomena and assuming that the high-frequency day-to-day variance is due to unpredictable independent noise. The differences between the semi-variograms become small for $\tau > 2$ days, which confirms that BAYESNF captures these longer-term temporal dependencies.

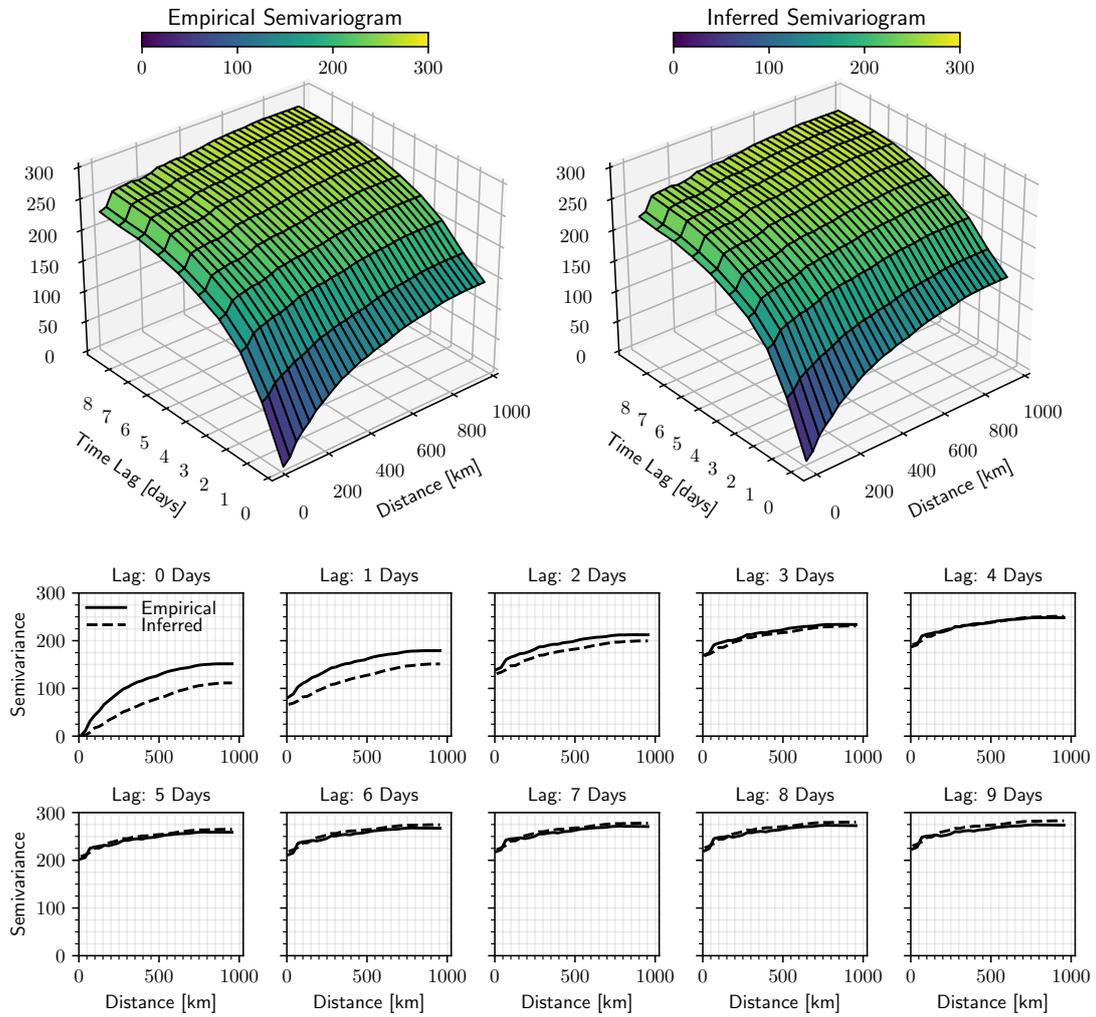


Fig. 3 Spatiotemporal variography for German PM10 air quality dataset. The empirical semivariogram is computed using the locations of the 70 stations. The inferred semivariogram is computed on 70 novel spatial locations sampled uniformly at random within the boundary of the field. The agreement between the surfaces indicates that BAYESNF extrapolates the joint spatiotemporal dependence structure between locations in the observed data to model the joint probability distribution of the field at arbitrary locations.

2.3 Prediction Accuracy on Scientific Datasets

Datasets

To quantitatively assess the effectiveness of BAYESNF, we curated a benchmark set comprised of six publicly available, large-scale spatiotemporal datasets that together cover a range of complex empirical processes.

1. Daily wind speed (km/h) from the Irish Meteorological Service [33].
1961-01-01 to 1978-12-31; 12 locations; 78,888 observations, 0% missing.
2. Daily particulate matter 10 (PM10) air quality in Germany from the European Environment Information and Observation Network [32].
1998-01-01 to 2009-12-31; 70 locations; 149,151 observations, 52% missing.
3. Hourly particulate matter 10 (PM10) from the London Air Quality Network [18].
2018-12-31 to 2019-03-31; 72 locations; 144,570 observations, 7% missing.
4. Weekly chickenpox cases from the Hungarian National Epidemiology Center [34].
2005-01-03 to 2014-12-29; 20 locations; 10,440 observation, 0% missing.
5. Monthly accumulated precipitation in Colorado and surrounding areas from the University Corporation for Atmospheric Research [35].
1950-01-01 to 1997-12-01; 358 locations; 134,800 observations, 35% missing.
6. Monthly sea surface temperature anomalies in the Pacific Ocean from the National Oceanic and Atmospheric Administration Climate Prediction Center [20].
1970-01-01 to 2003-03-01; 2261 locations; 902,139 observations, 0% missing.

Table 2 summarizes key statistics of these datasets. Figure 4 shows snapshots of the observed data at a fixed point in time (Fig. 4a) and in space (Fig. 4b), highlighting the complex statistical patterns (e.g., nonstationarity and periodicity) in the underlying fields along these two dimensions. Five train/test splits were created for each benchmark. The test sets contain $(\#locations)/(\#splits)$ locations, holding out the 10% most recent observations in temporal order.

Baselines

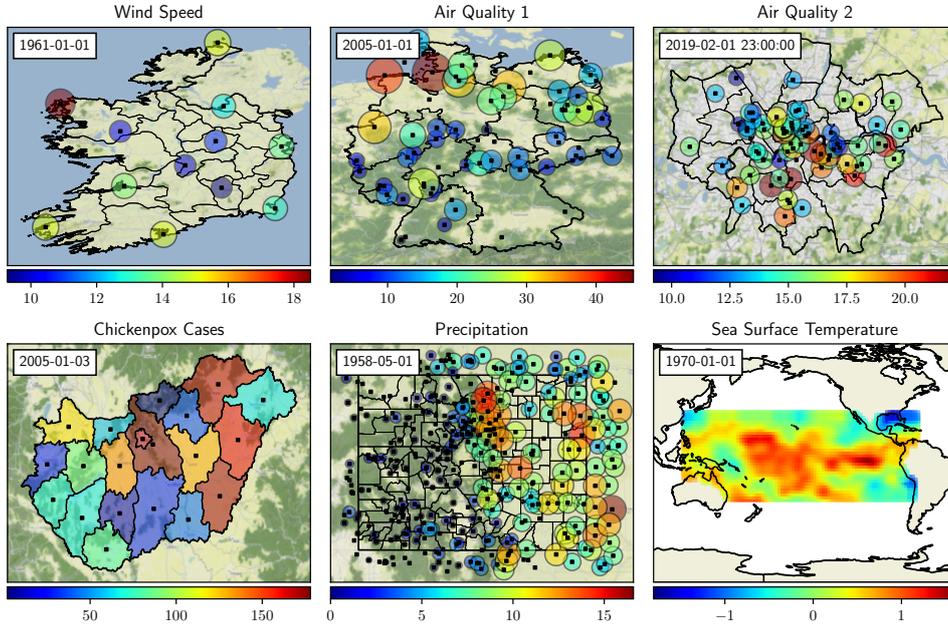
We compare the prediction accuracy on the benchmark datasets in Table 2 using BAYESNF and several state-of-the-art baselines that have quality open-source implementations and apply to domain-general spatiotemporal prediction problems:

1. SVGP: Spatiotemporal Sparse Variational Gaussian Process [18].
2. GBOOST (M): Spatiotemporal Gradient Boosting Trees (ensemble size M) [36].
3. TSREG: Trend Surface Regression with Ordinary Least Squares (OLS) [15, Sec. 3.2].
4. GLMM: Spatiotemporal Generalized Linear Mixed Effects Models [17], using
IID: Independent and identically distributed Gaussian errors.
AR1: Order 1 auto-regressive Gaussian errors.
RW: Gaussian random walk errors.
5. BAYESNF: Bayesian Neural Field; using the better of MAP or variational inference.
6. BAYESNF-NS: Same as above, without spatial Fourier features (9).

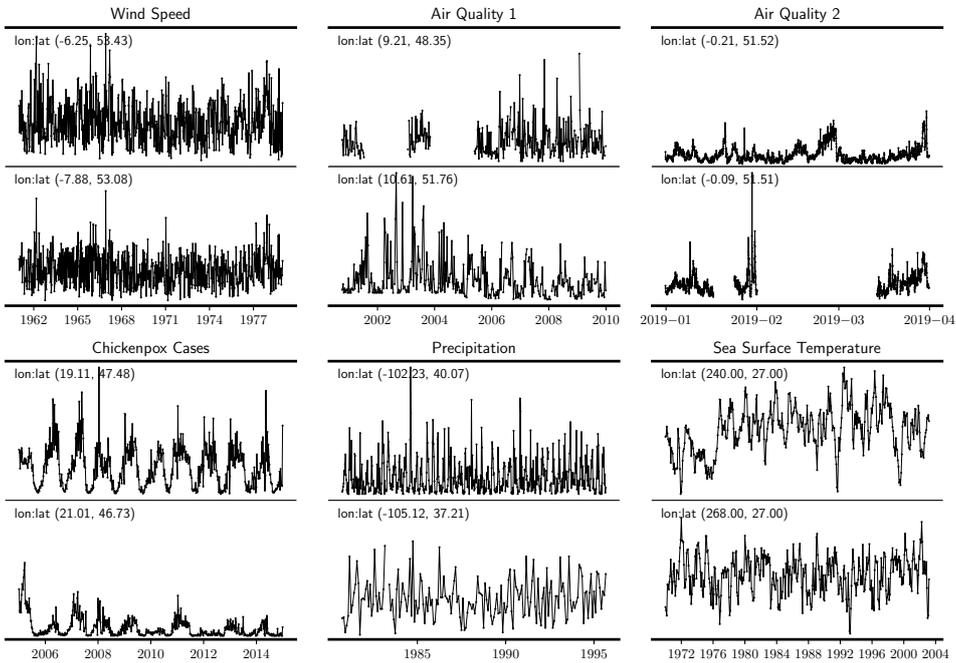
We also attempted to use the fixed-rank kriging (FRK) R baseline [20], but were unable to perform inference over noise parameters for spatiotemporal data. Taken together, the baselines provide broad coverage over recent statistical and machine learning methods for large-scale spatiotemporal prediction. To ensure a fair comparison, the same covariates $[x_1(\mathbf{s}, t), \dots, x_m(\mathbf{s}, t)]$ (5)–(9) provided to BAYESNF were also given to the TSREG and GBOOST baselines, which can easily incorporate custom features. All methods were run on a TPU v3-8 accelerator which consists of 8 cores each with 15.5 GiB of memory. Additional evaluation details are described in Section 4.

Table 2 Spatiotemporal datasets analyzed in empirical evaluation.

Dataset	Region	Frequency	Locations	Time Points	Observations	Missing	Start	End
Wind Speed	Ireland	Daily	12	6574	78,888	0%	1961-01-01	1978-12-31
Air Quality 1	Germany	Daily	70	4383	149,151	52%	1998-01-01	2009-12-31
Air Quality 2	London	Hourly	72	2159	144,570	7%	2018-12-31	2019-03-31
Chickenpox Cases	Hungary	Weekly	20	522	10,440	0%	2005-01-03	2014-12-29
Precipitation	Colorado	Monthly	358	576	134,800	35%	1950-01-01	1997-12-01
Sea Surface Temperature	Pacific Ocean	Monthly	2261	399	902,139	0%	1970-01-01	2003-03-01



(a) Snapshot of spatial observations at fixed time points.



(b) Snapshot of temporal observations at fixed locations (two per dataset).

Fig. 4 Spatial and temporal observations for evaluation datasets from Table 2.

Quantitative Results

Table 3 shows accuracy and runtime results for all baselines and benchmarks. Point predictions are evaluated using root-mean square error (RMSE (24)) and mean absolute error (MAE (25)) and 95% prediction intervals are evaluated using the mean interval score (MIS (26)), averaged over all train/test splits. The final column shows the wall-clock runtime in seconds that each method was run. While runtime cannot be perfectly aligned due to variety of learning algorithms used and their iterative nature, the wall-clock numbers show that all baselines were run for sufficiently long to ensure a fair comparison. Figure 5 compares predictions on held-out data at one representative spatial location in each of the six benchmarks. We discuss several takeaways from these results.

BAYESNF is the strongest baseline (in terms of RMSE, MAE, MIS) in 15/18 cases: the improvements over the next-best non-BAYESNF baseline are statistically significant in all 15 cases (Mann-Whitney U-Test, 5% level with Bonferroni correction). In 3/18 cases (Air Quality 1, MAE; Chickenpox, MAE and RMSE) the errors from BAYESNF are slightly higher than another baseline: however, only 1/15 are statistically significant and the running times of the top baselines are $\sim 10x$ and $\sim 4x$ higher than BAYESNF. The most apparent improvements of BAYESNF occur in the Wind Speed, Precipitation, and Sea Surface Temperature datasets, shown qualitatively in rows 1, 5, 6 of Fig. 5. Omitting spatial Fourier features (BAYESNF-NS baseline) generally gives worse results that are not always competitive with the baselines. These findings highlight the expressive modeling capacity of BAYESNF, their ability to accurately quantify predictive uncertainty, and the benefit of using spatial embeddings to capture high-frequency signals.

While predictions from SVGP generally follow the overall “shape” of the held-out data, the mean estimates and prediction intervals are not well calibrated (Fig. 5, second column). SVGP requires several modeling trade-offs to ensure linear-time scaling in the number of time points, specifically the use of (i) Matérn kernels, which are not always appropriate (e.g., they cannot capture seasonal effects); and (ii) kernels that are separable in time and space. Additional difficulties with the method include manually selecting the number of spatial inducing points and complex algorithms needed to optimize their locations. SVGP also runs out of memory on the Sea Surface Temperature benchmark, which has around 1 million observations.

The GLMM methods (AR1, IID, RW), which use stochastic partial differential equations for scaling up the Gaussian random field error models, fail to complete on 4/6 benchmarks. The scaling characteristics are also unpredictable: for example, GLMM runs on Air Quality 2 (144,570 observations) but fails on Wind Speed (78,888 observations). On the two datasets they can handle (rows 3 and 4 of Fig. 5), the GLMM methods are highly competitive on Chickenpox and not competitive on Air Quality 2, with the AR1 variant delivering the lowest errors.

GBOOST is a reliable and easy-to-use method that delivers reasonable prediction intervals, but its point predictions underfit (Fig. 5, third column). It has a high computational cost for two reasons. First, a large number of estimators is needed to obtain accurate predictions: the prediction accuracy improvements from $M = 500$ to $M = 1000$ estimators confirm that large values of M are needed. Second, GBOOST must be retrained from scratch three times, once to obtain a model that predicts the mean and twice to obtain the models that predict the upper and lower quantiles. Unlike BAYESNF, which uses a single learned distribution for all queries, fitting different models for each query in GBOOST does not guarantee probabilistically coherent results.

TSREG requires less than 1 second to deliver a result, which is $100x$ – $1000x$ faster than the other methods. However, it fails to capture any meaningful structure and produces poor predictions. Using LASSO or ridge regression instead of OLS did not provide an improvement. TSREG uses identical covariates to BAYESNF but performs much worse, which highlights the presence of nonlinear dependencies in the data that are used to produce accurate forecasts.

Table 3 Point prediction errors (RMSE, MAE), interval prediction error (MIS), and wall-clock runtime (in seconds) on spatiotemporal benchmark datasets for multiple baselines methods. Each measurement is an average over five independent test/train splits. The symbol \times denotes an experiment that failed to complete successfully (time-out, out-of-memory, etc.). Italics indicate lowest RMSE, asterisk lowest MAE, and bold lowest MIS. Underlined values are significantly lower than the next-best (Mann-Whitney U-Test, 5% level with Bonferroni correction).

Dataset	Method	Prediction Error			Runtime
		RMSE	MAE	MIS	
Wind Speed	<i>Bayesian Neural Field*</i>	<u>2.44</u>	<u>1.80</u>	<u>11.89</u>	1289
	Bayesian Neural Field (No Spatial Features)	2.67	1.98	13.72	866
	Sparse Spatiotemporal Variational Gaussian Process	5.04	4.18	24.72	1112
	Spatiotemporal Gradient Boosting Trees (1000)	3.74	2.79	18.43	2907
	Spatiotemporal Gradient Boosting Trees (500)	4.06	3.09	19.05	1474
	Spatiotemporal Generalized Linear Mixed Model (All)	\times	\times	\times	\times
	Trend Surface Regression	4.94	3.88	24.83	1
Air Quality 1	<i>Bayesian Neural Field</i>	<u>5.36</u>	3.25	<u>25.38</u>	354
	Bayesian Neural Field (No Spatial Features)	5.71	3.49	29.54	151
	Sparse Spatiotemporal Variational Gaussian Process*	6.24	<u>2.91</u>	35.59	1348
	Spatiotemporal Gradient Boosting Trees (1000)	7.42	4.40	31.56	5665
	Spatiotemporal Gradient Boosting Trees (500)	7.97	4.80	33.26	2843
	Spatiotemporal Generalized Linear Mixed Model (All)	\times	\times	\times	\times
	Trend Surface Regression	9.35	6.62	55.98	1
Air Quality 2	<i>Bayesian Neural Field*</i>	<u>8.44</u>	<u>5.19</u>	<u>41.48</u>	366
	Bayesian Neural Field (No Spatial Features)	9.03	5.89	50.89	185
	Sparse Spatiotemporal Variational Gaussian Process	9.92	6.78	56.12	628
	Spatiotemporal Gradient Boosting Trees (1000)	8.77	5.57	43.71	2671
	Spatiotemporal Gradient Boosting Trees (500)	9.02	5.74	44.69	1374
	Spatiotemporal Generalized Linear Mixed Model (AR1)	11.92	7.81	73.00	17100
	Spatiotemporal Generalized Linear Mixed Model (RW)	14.62	9.48	157.10	9447
	Spatiotemporal Generalized Linear Mixed Model (IID)	12.87	8.78	127.48	3545
	Trend Surface Regression	18.44	12.32	117.90	1
Chickenpox Cases	Bayesian Neural Field	25.19	15.89	<u>112.63</u>	70
	Bayesian Neural Field (No Spatial Features)	28.98	18.88	152.63	63
	Sparse Spatiotemporal Variational Gaussian Process	32.00	21.22	212.87	63
	Spatiotemporal Gradient Boosting Trees (1000)	26.83	15.84	122.39	189
	Spatiotemporal Gradient Boosting Trees (500)	26.89	15.84	119.27	93
	<i>Spatiotemporal Generalized Linear Mixed Model (AR1)*</i>	25.30	15.26	179.29	887
	Spatiotemporal Generalized Linear Mixed Model (RW)	26.92	16.79	179.63	386
	Spatiotemporal Generalized Linear Mixed Model (IID)	28.23	16.85	327.72	264
	Trend Surface Regression	29.75	21.30	172.43	1
Precipitation	<i>Bayesian Neural Field*</i>	<u>1.87</u>	<u>1.29</u>	<u>8.88</u>	357
	Bayesian Neural Field (No Spatial Features)	1.90	1.24	10.53	254
	Sparse Spatiotemporal Variational Gaussian Process	3.14	2.27	31.00	1203
	Spatiotemporal Gradient Boosting Trees (1000)	2.63	1.67	11.13	2064
	Spatiotemporal Gradient Boosting Trees (500)	2.82	1.81	11.54	1038
	Spatiotemporal Generalized Linear Mixed Model (All)	\times	\times	\times	\times
	Trend Surface Regression	3.61	2.69	20.81	1
Sea Surface Temperature	<i>Bayesian Neural Field*</i>	<u>0.10</u>	<u>0.06</u>	<u>0.64</u>	2400
	Bayesian Neural Field (No Spatial Features)	0.14	0.08	0.86	2294
	Sparse Spatiotemporal Variational Gaussian Process	\times	\times	\times	\times
	Spatiotemporal Gradient Boosting Trees (1000)	0.45	0.33	1.94	12379
	Spatiotemporal Gradient Boosting Trees (500)	0.49	0.37	2.23	2258
	Spatiotemporal Generalized Linear Mixed Model (All)	\times	\times	\times	\times
	Trend Surface Regression	0.55	0.42	2.89	3

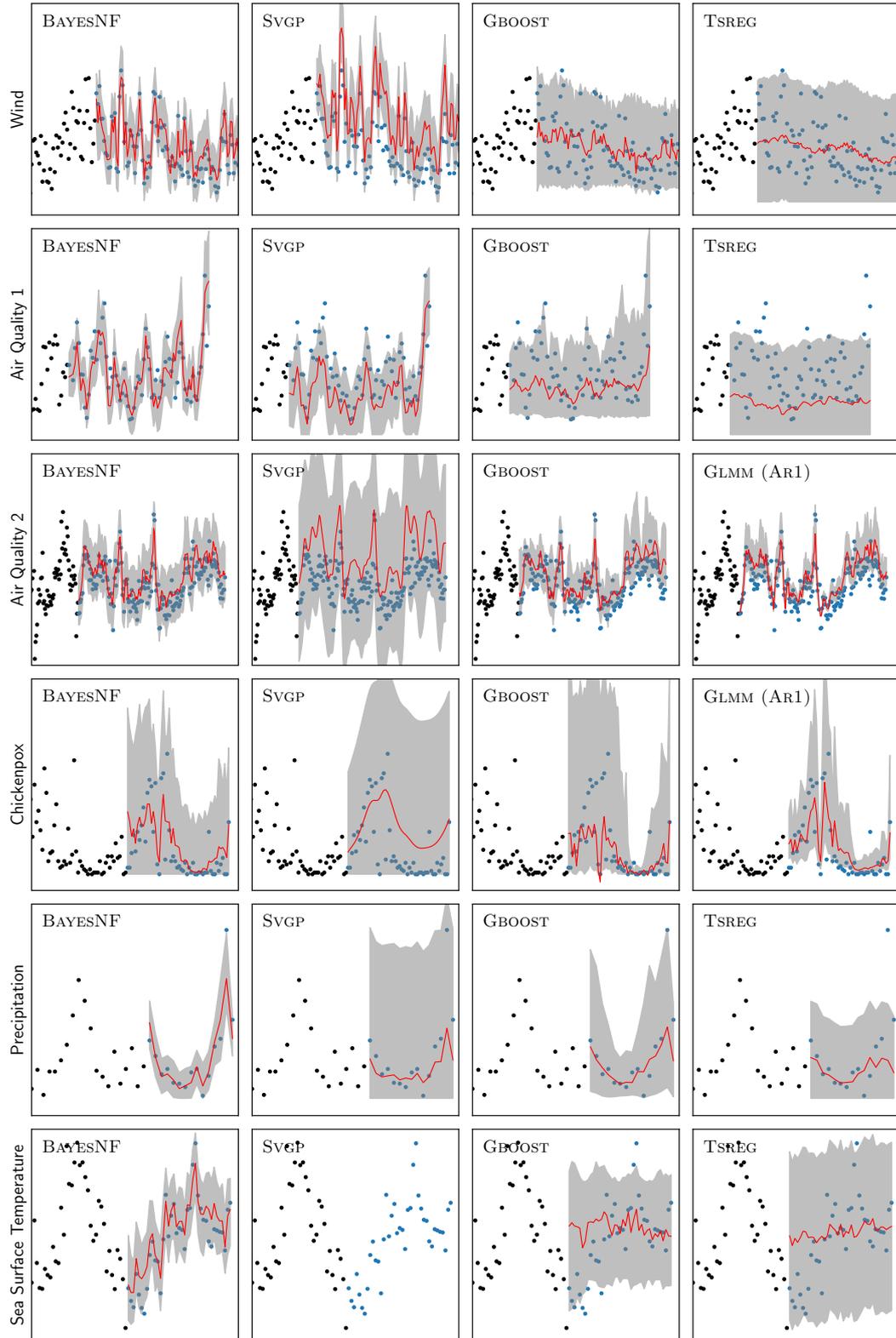


Fig. 5 Comparison of predictions using BAYESNF and various baselines. Each row shows results for a given spatiotemporal benchmark dataset at one spatial location. Black dots are observed data, blue dots are test data, red lines are median forecasts, and gray regions are 95% prediction intervals.

3 Discussion

This article has introduced the Bayesian Neural Field—a novel probabilistic framework for scalable spatiotemporal prediction. The model combines a novel deep neural network architecture for high-capacity function approximation with multilevel Bayesian modeling for accurate uncertainty estimation over complex spatiotemporal fields. Posterior inference is conducted using stochastic ensembles of maximum a-posterior estimation or variationally trained surrogates, which are easy to apply and deliver well-calibrated prediction intervals. Additional advantages of BAYESNF are its (relative) simplicity, ability to handle missing data, and ability to learn a full probability distribution over arbitrary space-time indexes within the spatiotemporal field.

We performed a comprehensive evaluation of BAYESNF against strong statistical and machine learning baselines on real-world scientific datasets containing tens to hundreds of thousands of observations. The results show significant improvements in both point and interval forecasts. The results also show that combining periodic effects in the temporal domain with Fourier features in the spatial domain enables BAYESNF to express spatiotemporal structure with multiple (non-integer) periodicity and high-frequency components. The flexibility of BAYESNF enables it to produce strong results across multiple problems without complex dataset-specific modeling or inference approximations, which are typically needed to apply other techniques such as Gaussian processes or generalized linear-mixed effect models to large spatiotemporal data. For a representative air quality dataset, the semi-variograms inferred by BAYESNF evaluated at novel spatial locations agree with the empirical semi-variogram computed at observed locations, which highlights the model’s ability to generalize effectively in space and time.

Practitioners across a spectrum of disciplines—from meteorology to urban studies and environmental informatics—are in need of more scalable and easy-to-use statistical methods for spatiotemporal prediction. A freely available implementation of BAYESNF built on the JAX machine learning platform, along with user documentation and tutorials, is available at <https://github.com/google/bayesnf>. We hope these materials help practitioners obtain strong BAYESNF models for many spatiotemporal problems that existing software cannot easily handle.

The approach discussed in this paper opens several avenues to future work. While Bayesian Neural Fields are designed to minimize the user’s involvement in constructing a predictive model, further improvements can be achieved by enabling domain experts to incorporate specific statistical covariance structure that they know to be present. It is also worthwhile to explore applications of BAYESNF for modeling the residuals of causal or mechanistic laws in physical systems where there exist strong domain theories of the average data-generating process, but poor models of the empirical noise process. Another promising extension is using BAYESNF models to handle not only “geostatistical” datasets, in which the measurements are point-referenced in space, but also “areal” or “lattice” datasets, where the measurements represent aggregated quantities over a geographical region. While areal datasets are often converted to geostatistical datasets by using the centroid of the region as the representative point, a more principled approach would be to compute the integral a Bayesian Neural Field over the region. Finally, BAYESNF can be generalized to handle multivariate spatiotemporal data, where each spatial location is associated with multiple time series that contain within-location and across-location covariance structure. Effectively handling such datasets will even further broaden the scope of problems that BAYESNF can solve.

4 Methods

4.1 Posterior Inference

Let $P(\Theta_f, \Theta_y, Y)$ denote the joint probability distribution over the parameters and observable field in Listing 1. The posterior distribution is given by Eq. (13) in the main text. We describe two approximate posterior inference algorithms for BAYESNF. In these sections, we define $\Theta = (\Theta_f, \Theta_y)$, $\theta = (\theta_f, \theta_y)$ and $\mathbf{r} = (\mathbf{s}, t)$.

Stochastic MAP Ensembles

A simple approach to uncertainty quantification is based on the “maximum a-posteriori” estimate:

$$\begin{aligned}\theta^* &= \arg \max_{\theta} \left\{ \log P(\theta_f \theta_y \mid \{Y(\mathbf{r}_i) = y(\mathbf{r}_i)\}_{i=1}^N) \right\} \\ &= \arg \max_{\theta} \left\{ \log P(\theta_f, \theta_y, \{Y(\mathbf{r}_i) = y(\mathbf{r}_i)\}_{i=1}^N) \right\}.\end{aligned}\quad (15)$$

We find an approximate solution to the optimization problem (16) using stochastic gradient ascent on the joint log probability, according to the procedure in Listing 2, where $B \leq N$ is a mini-batch size and $(\epsilon_1, \epsilon_2, \dots)$ is a sequence of learning rates.

Initialize $\theta_0 \sim \pi_f \pi_y$; $t \leftarrow 0$ Repeat until convergence $\{I_1, \dots, I_B\} \sim \text{Uniform}(\{K \subset [N] \mid \text{card}(K) = B\})$	(16)
$\hat{g}_t = \nabla_{\theta} \left[\log \pi_f(\theta_f) + \log \pi_y(\theta_y) + \frac{N}{B} \sum_{j=1}^B \log (\text{Dist}(y(\mathbf{r}_{I_j}); F_{\theta_f}(\mathbf{r}_{I_j}), \theta_y)) \right]_{\theta_{t-1}}$	(17)
$\theta_t = \theta_{t-1} + \epsilon_t \hat{g}_t$; $t \leftarrow t + 1$,	(18)

Listing 2 Stochastic MAP estimation for Bayesian Neural Field.

We construct an overall “deep ensemble” $\{(\theta_f^i, \theta_y^i)\}_{i=1}^M$ containing $M \geq 1$ MAP estimates by repeating the above procedure M times, each with a different initialization of θ_0 and random seed.

Stochastic Variational Inference

A more uncertainty-aware alternative to MAP ensembles is mean-field variational inference, which uses a surrogate posterior $q_{\phi}(\theta) = \prod_{i=1}^{n_f} \nu(\theta_{f,i}; \phi_{f,i}) \prod_{i=1}^{n_y} \nu(\theta_{y,i}; \phi_{y,i})$ over Θ to approximate the true posterior $P(\theta_f, \theta_y \mid \mathcal{D})$ (13) given the data \mathcal{D} . Optimal values for the variational parameters $\phi = (\phi_{f,1}, \dots, \phi_{f,n_f}, \phi_{y,1}, \dots, \phi_{y,n_y})$ are obtained by maximizing the “evidence lower bound”:

$$\text{ELBO}(\phi) = \log P(\mathcal{D}) - \text{KL}(q_{\phi}(\theta) \parallel P(\theta \mid \mathcal{D})) = \mathbb{E}_{\phi} \left[\log \frac{P(\mathcal{D}, \theta)}{q_{\phi}(\theta)} \right] \quad (19)$$

$$= \mathbb{E}_{\phi} [\log P(\mathcal{D} \mid \theta)] - \text{KL}(q_{\phi}(\theta) \parallel \pi(\theta)). \quad (20)$$

Assuming independent priors we have

$$\begin{aligned}&= \sum_{i=1}^N \mathbb{E}_{\phi} [\log (\text{Dist}(y(\mathbf{r}_i); F_{\theta_f}(\mathbf{r}_i), \theta_y))] \\ &\quad - \sum_{i=1}^{n_f} \mathbb{E}_{\phi_{f,i}} \left[\log \left(\frac{\nu(\theta_{f,i}; \phi_{f,i})}{\pi_f(\theta_{f,i})} \right) \right] - \sum_{i=1}^{n_y} \mathbb{E}_{\phi_{y,i}} \left[\log \left(\frac{\nu(\theta_{y,i}; \phi_{y,i})}{\pi_y(\theta_{y,i})} \right) \right].\end{aligned}\quad (21)$$

Finding the maximum of Eq. (21) is a challenging optimization problem. Our implementation leverages a Gaussian variational posterior q_{ϕ} with KL reweighting, as described in Blundell et al. [37, Sec. 3.2, 3.4].

Mean-field variational inference is known to underestimate posterior variance and can also get stuck in local optima of Eq. (20). To alleviate both of these problems, we propose using a *variational ensemble* that is analogous to the MAP ensemble described above. More specifically, we first perform $M \geq 1$ runs of stochastic variational inference with different initializations and random seeds, which gives us an ensemble $\{\phi^i, i = 1, \dots, M\}$ of variational parameters. We then

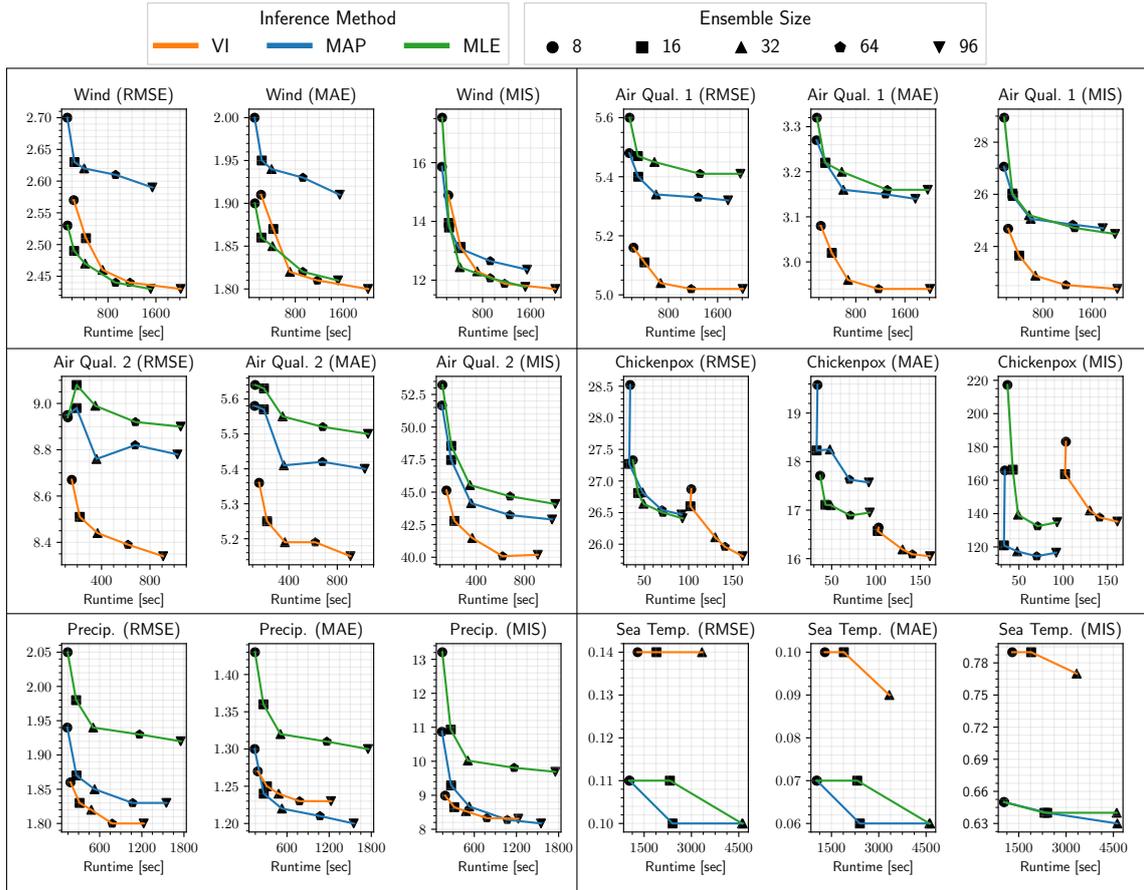


Fig. 6 Runtime vs. prediction error profiles using VI (orange) and MAP (blue) inference for BAYESNF on the spatiotemporal benchmarks from Table 2. Markers indicate ensemble size (8, 16, 32, 64, 96).

approximate the posterior $P(\theta | D)$ with an equal-weighted mixture of the resulting variational distributions $\{q_{\phi^i}\}_{i=1}^M$.

Comparison of MAP, VI, and MLE

Figure 6 shows a comparison of runtime vs. accuracy profiles on the six benchmarks from Table 2 using three parameter inference methods for BAYESNF—MAP, VI, and MLE. The first two are described in Section 4.1. MLE is the maximum likelihood estimation baseline described in Lakshminarayanan et al. [38], which is identical to Listing 1 except that the terms π_f and π_y in Eq. (17) are ignored. MLE performs no better than MAP or VI in all 18/18 profiles (and is typically worse), illustrating the benefits of parameter priors and posterior uncertainty which do not impose runtime overhead. Between MAP and VI, the latter performs better in 13/18 profiles: that is, on all metrics for Wind, Air Quality 1, and Air Quality 2; on RMSE and MAE for Chickenpox; and on RMSE and MIS for Precipitation.

4.2 Prediction Queries

We can approximate the posterior (13) using a set of samples $\{(\theta_f^i, \theta_y^i)\}_{i=1}^M$, which may be obtained from either MAP ensemble estimation or stochastic variational inference (by sampling from the

ensemble of M variational distributions). We can then approximate the posterior-predictive distribution $P(Y(\mathbf{r}_*) | \mathcal{D})$ (which marginalizes out the parameters Θ) of $Y(\mathbf{r}_*)$ at a novel field index $\mathbf{r}_* = (\mathbf{s}_*, t_*)$ by a mixture model with M equally weighted components:

$$\hat{P}(Y(\mathbf{r}_*) | \mathcal{D}) = \frac{1}{M} \sum_{i=1}^M \text{Dist}(Y(\mathbf{r}_*); F_{\theta_f^i}(\mathbf{r}_*), \theta_y^i). \quad (22)$$

Equipped with Eq. (22), we can directly compute predictive probabilities of events $\{Y(\mathbf{r}_*) \leq y\}$, predictive probability densities $\{Y(\mathbf{r}_*) = y\}$, or conditional expectations $\mathbb{E}[\varphi(Y(\mathbf{r}_*)) | \mathcal{D}]$ for a probe function $\varphi : \mathbb{R} \rightarrow \mathbb{R}$. Prediction intervals around $Y(\mathbf{r}_*)$ are estimated by computing the α -quantile $y_\alpha(\mathbf{r}_*)$, which satisfies

$$\hat{P}(Y(\mathbf{r}_*) \leq y_\alpha(\mathbf{r}_*) | \mathcal{D}) = \alpha \quad \alpha \in [0, 1]. \quad (23)$$

For example, the median estimate is $y_{0.50}(\mathbf{s}_*, t_*)$ and 95% prediction interval is $[y_{0.025}(\mathbf{s}_*, t_*), y_{0.975}(\mathbf{s}_*, t_*)]$. The quantiles (23) are estimated numerically using Chandrupatla’s root finding algorithm [39] on the cumulative distribution function of the mixture (22).

4.3 Evaluation Metrics

In Section 2.3, the quality of point forecasts are evaluated using the RMSE and MAE score and interval forecasts at level $\alpha = 0.05$ using the MIS score:

$$\text{Root Mean Squared Error (RMSE)} \quad \sqrt{\sum_{i=1}^n (y_i - \hat{y}_i)^2 / n} \quad (24)$$

$$\text{Mean Absolute Error (MAE)} \quad \sum_{i=1}^n |y_i - \hat{y}_i| / n \quad (25)$$

$$\begin{aligned} \text{Mean Interval Score (MIS)} \quad & \sum_{i=1}^n \left[(u_i - \ell_i) + \frac{2}{\alpha} (\ell_i - y_i) \mathbf{1}[y_i < \ell_i] \right. \\ & \left. + \frac{2}{\alpha} (y_i - u_i) \mathbf{1}[u_i < y_i] \right] / n. \end{aligned} \quad (26)$$

Availability of Code & Data

An open-source Python implementation of BAYESNF is available at <https://github.com/google/bayesnf> under an Apache-2.0 License. The full evaluation pipeline containing all model configurations for the baselines is also provided in the repository.

All datasets analyzed in Section 2.3 (Table 2) are publicly available under open-source licenses.

- Wind Speed. GNU GPL v2. <https://r-spatial.github.io/gstat/reference/wind.html>.
- Air Quality 1. GNU GPL v3. <https://rdr.io/cran/spacetime/man/air.html>.
- Air Quality 2. CC Attribution 1.0 Generic. <https://doi.org/10.5281/zenodo.4531304>.
- Chickenpox Cases. CC Attribution 4.0 International. <https://doi.org/10.24432/C5103B>.
- Precipitation. Public Domain. <https://www.image.ucar.edu/Data/US.monthly.met/>.
- Sea Surface Temperature. GNU GPL v2. <https://github.com/andrewzm/STRbook/>.

The train/test splits used to produce Table 3 are available at <https://www.cs.cmu.edu/~fsaad/assets/bayesnf/datasets.tar.gz>. The predictions of all the baselines on the test data are available at <https://www.cs.cmu.edu/~fsaad/assets/bayesnf/results.tar.gz>. Refer to the README in these files for instructions.

References

- [1] Wang, S., Yuan, W., Shang, K.: The impacts of different kinds of dust events on PM10 pollution in northern China. *Atmospheric Environment* **40**(40), 7975–7982 (2006) <https://doi.org/10.1016/j.atmosenv.2006.06.058>
- [2] Medina, S., Plasencia, A., Ballester, F., Mücke, H.G., Schwartz, J.: Apheis: Public health impact of PM10 in 19 European cities. *Journal of Epidemiology & Community Health* **58**(10), 831–836 (2004) <https://doi.org/10.1136/jech.2003.016386>
- [3] Huang, W., Li, T., Liu, J., Xie, P., Du, S., Teng, F.: An overview of air quality analysis by big data techniques: Monitoring, forecasting, and traceability. *Information Fusion* **75**, 28–40 (2021) <https://doi.org/10.1016/j.inffus.2021.03.010>
- [4] Karagulian, F., Barbieri, M., Kotsev, A., Spinelle, L., Gerboles, M., Lagler, F., Redon, N., Crunaire, S., Borowiak, A.: Review of the performance of low-cost sensors for air quality monitoring. *Atmosphere* **10**(9), 506 (2019) <https://doi.org/10.3390/atmos10090506>
- [5] Niu, D., Feng, C., Li, B.: Pricing cloud bandwidth reservations under demand uncertainty. In: *Proceedings of the 12th ACM SIGMETRICS/PERFORMANCE Joint International Conference on Measurement and Modeling of Computer Systems*. Association for Computing Machinery, New York, NY, USA (2012). <https://doi.org/10.1145/2254756.2254776> . <https://doi.org/10.1145/2254756.2254776>
- [6] Mishra, S.K., Sahoo, B., Paramita Parida, P.: Load balancing in cloud computing: A big picture. *Journal of King Saud University - Computer and Information Sciences* **32**(2), 149–158 (2020) <https://doi.org/10.1016/j.jksuci.2018.01.003>
- [7] Cao, J., Wu, Y., Li, M.: Energy efficient allocation of virtual machines in cloud computing environments based on demand forecast. In: Li, R., Cao, J., Bourgeois, J. (eds.) *Advances in Grid and Pervasive Computing*. Lecture Notes in Computer Science, vol. 7296, pp. 137–151. Springer, Berlin, Heidelberg (2012)
- [8] Faniyi, F., Bahsoon, R.: A systematic review of service level management in the cloud. *ACM Comput. Surv.* **48**(3), 43–127 (2015) <https://doi.org/10.1145/2843890>
- [9] Sigrist, F., Künsch, H.R., Stahel, W.A.: A dynamic nonstationary spatio-temporal model for short term prediction of precipitation. *The Annals of Applied Statistics* **6**(4), 1452–1477 (2012) <https://doi.org/10.1214/12-AOAS564>
- [10] Jung, J., Broadwater, R.P.: Current status and future advances for wind speed and power forecasting. *Renewable and Sustainable Energy Reviews* **31**, 762–777 (2014) <https://doi.org/10.1016/j.rser.2013.12.054>
- [11] Lu, F.S., Hattab, M.W., Clemente, C.L., Biggerstaff, M., Santillana, M.: Improved state-level influenza nowcasting in the United States leveraging internet-based data and network approaches. *Nature Communications* **10**(147) (2019) <https://doi.org/10.1038/s41467-018-08082-0>
- [12] Gan, Z., Yang, M., Feng, T., Timmermans, H.: Understanding urban mobility patterns from a spatiotemporal perspective: daily ridership profiles of metro stations. *Transportation* **47**, 315–336 (2020) <https://doi.org/10.1007/s11116-018-9885-4>

- [13] Rasmussen, C.E., Williams, C.K.I.: Gaussian Processes for Machine Learning. The MIT Press, Cambridge, MA (2006)
- [14] Cressie, N., Wikle, C.K.: Statistics for Spatio-temporal Data. Wiley Series in Probability and Statistics. John Wiley & Sons, New York, NY (2011)
- [15] Wikle, C.K., Zammit-Mangion, A., Cressie, N.: Spatio-Temporal Statistics with R. Chapman and Hall/CRC, Boca Raton, FL (2019). <https://doi.org/10.1201/9781351769723>
- [16] Rue, H., Riebler, A., Sørbye, S.H., Illian, J.B., Simpson, D.P., Lindgren, F.K.: Bayesian computing with inla: A review. *Annual Review of Statistics and Its Application* **4**(1), 395–421 (2017) <https://doi.org/10.1146/annurev-statistics-060116-054045>
- [17] Anderson, S.C., Ward, E.J., English, P.A., K., B.L.A.: sdmTMB: An R package for fast, flexible, and user-friendly generalized linear mixed effects models with spatial and spatiotemporal random fields. *bioRxiv* (2022) <https://doi.org/10.1101/2022.03.24.485545>
- [18] Hamelijncck, O., Wilkinson, W., Loppi, N., Solin, A., Damoulas, T.: Spatio-temporal variational Gaussian processes. In: Proceedings of the 35th Conference on Neural Information Processing Systems. *Advances in Neural Information Processing Systems*, vol. 34. Curran Associates, Inc., Red Hook, NY (2021)
- [19] Zhang, J., Ju, Y., Mu, B., Zhong, R., Chen, T.: An efficient implementation for spatial-temporal Gaussian process regression and its applications. *Automatica* **147**(110679) (2023) <https://doi.org/10.1016/j.automatica.2022.110679>
- [20] Zammit-Mangion, A., Cressie, N.: FRK: An R package for spatial and spatio-temporal prediction with large datasets. *Journal of Statistical Software* **98**(4), 1–48 (2021) <https://doi.org/10.18637/jss.v098.i04>
- [21] Banerjee, S.: Modeling massive spatial datasets using a conjugate Bayesian linear modeling framework. *Spatial Statistics* **37**, 100417 (2020) <https://doi.org/10.1016/j.spasta.2020.100417>
- [22] Wikle, C.K., Zammit-Mangion, A.: Statistical deep learning for spatial and spatiotemporal data. *Annual Review of Statistics and Its Application* **10**(1), 247–270 (2023) <https://doi.org/10.1146/annurev-statistics-033021-112628>
- [23] McDermott, P.L., Wikle, C.K.: Bayesian recurrent neural network models for forecasting and quantifying uncertainty in spatial-temporal data. *Entropy* **21**(2), 184–125 (2019) <https://doi.org/10.3390/e21020184>
- [24] Amato, F., Guignard, F., Sylvain, R., Kanevski, M.: A novel framework for spatio-temporal prediction of environmental data using deep learning. *Nature Scientific Reports* **10**(22243) (2020) <https://doi.org/10.1038/s41598-020-79148-7>
- [25] Vu, Q., Zammit-Mangion, A., Chuter, S.J.: Constructing large nonstationary spatio-temporal covariance models via compositional warpings. *Spatial Statistics* **54**, 100742 (2023) <https://doi.org/10.1016/j.spasta.2023.100742>
- [26] Neal, R.M.: Bayesian learning for neural networks. PhD thesis, University of Toronto (1996)
- [27] Mildenhall, B., Srinivasan, P.P., Tancik, M., Barron, J.T., Ramamoorthi, R., Ng, R.: Nerf:

Representing scenes as neural radiance fields for view synthesis. *Communications of the ACM* **65**(1), 99–106 (2021)

- [28] Hoffman, M.D., Le, T.A., Soutsov, P., Suter, C., Lee, B., Mansinghka, V.K., Saurous, R.A.: Probnerrf: Uncertainty-aware inference of 3D shapes from 2D images. In: *International Conference on Artificial Intelligence and Statistics*, pp. 10425–10444 (2023). PMLR
- [29] Tancik, M., Srinivasan, P., Mildenhall, B., Fridovich-Keil, S., Raghavan, N., Singhal, U., Ramamoorthi, R., Barron, J., Ng, R.: Fourier features let networks learn high frequency functions in low dimensional domains. *Advances in Neural Information Processing Systems* **33**, 7537–7547 (2020)
- [30] LeCun, Y.A., Bottou, L., Orr, G.B., Müller, K.-R.: Efficient backprop. In: Montavon, G., Orr, G.B., Müller, K.-R. (eds.) *Neural Networks: Tricks of the Trade: Second Edition*, pp. 9–48. Springer, Berlin (2012). https://doi.org/10.1007/978-3-642-35289-8_3
- [31] Pearce, T., Tsuchida, R., Zaki, M., Brintrup, A., Neely, A.: Expressive priors in bayesian neural networks: Kernel combinations and periodic functions. In: *Proceedings of The 35th Uncertainty in Artificial Intelligence Conference*. *Proceedings of Machine Learning Research*, vol. 115, pp. 134–144. PMLR, ??? (2020)
- [32] Pebesma, E.: spacetime: Spatio-temporal data in R. *Journal of Statistical Software* **51**(7), 1–30 (2012) <https://doi.org/10.18637/jss.v051.i07>
- [33] Haslett, J., Raftery, A.E.: Space-time modelling with long-memory dependence: Assessing Ireland’s wind power resource. *Journal of the Royal Statistical Society. Series C (Applied Statistics)* **38**(1), 1–50 (1989) <https://doi.org/10.2307/2347679>
- [34] Hungarian Chickenpox Cases. UCI Machine Learning Repository (2021). <https://doi.org/10.24432/C5103B>
- [35] US Precipitation and Temperature Data 1895–1997. University Corporation for Atmospheric Research (2010). <https://www.image.ucar.edu/Data/US.monthly.met/>
- [36] Pedregosa, F., *et al.*: Scikit-learn: Machine learning in Python. *Journal of Machine Learning Research* **12**, 2825–2830 (2011)
- [37] Blundell, C., Cornebise, J., Kavukcuoglu, K., Wierstra, D.: Weight uncertainty in neural networks. In: *Proceedings of the 32nd International Conference on Machine Learning*. *Proceedings of Machine Learning Research*, vol. 37, pp. 1613–1622. PMLR, Lille, France (2015)
- [38] Lakshminarayanan, B., Pritzel, A., Blundell, C.: Simple and scalable predictive uncertainty estimation using deep ensembles. In: *Proceedings of the 31st Conference on Neural Information Processing Systems*. *Advances in Neural Information Processing Systems*, vol. 30. Curran Associates, Inc., Red Hook, NY (2017)
- [39] Chandrupatla, T.R.: A new hybrid quadratic/bisection algorithm for finding the zero of a nonlinear function without using derivatives. *Advances in Engineering Software* **28**(3), 145–149 (1997) [https://doi.org/10.1016/S0965-9978\(96\)00051-8](https://doi.org/10.1016/S0965-9978(96)00051-8)